

Production and polarization of direct J/ψ to $\mathcal{O}(\alpha_s^3)$ in the improved color evaporation model in collinear factorization

Vincent Cheung*

Department of Physics and Astronomy, University of California, Davis, Davis, California 95616, USA

Ramona Vogt

*Nuclear and Chemical Sciences Division, Lawrence Livermore National Laboratory, Livermore, California 94551, USA and
Department of Physics and Astronomy, University of California, Davis, Davis, California 95616, USA*

(Dated: February 13, 2022)

We calculate the production and polarization of direct J/ψ in the improved color evaporation model at $\mathcal{O}(\alpha_s^3)$ in the collinear factorization approach. We present the first calculation of polarization parameters λ_ϑ , λ_φ , and $\lambda_{\vartheta\varphi}$ in the helicity and the Collins-Soper frames, as well as the frame-invariant polarization parameter $\tilde{\lambda}$ as a function of transverse momentum. We find agreement with both J/ψ cross sections and the invariant polarization parameters at small and moderate p_T .

I. INTRODUCTION

Quarkonium production is important to understand both the long- and short-distance aspects of QCD. Both the perturbative and nonperturbative natures of QCD are needed to model the production of quarkonium from heavy quark production in hard processes to the hadronization of the final state. Nonrelativistic QCD (NRQCD) [1], the most commonly employed model of quarkonium production cannot describe the J/ψ production and polarization while respecting the universality of the long-distance matrix elements for p_T cuts less than twice the mass of the quarkonium state [2, 3]. It also has difficulty describing the J/ψ polarization and the LHCb η_c production [4, 5] while using heavy quark spin symmetry [6–8]. On the other hand, the color evaporation model (CEM) [9–11] and the improved CEM (ICEM) [12] have only been employed extensively to hadroproduction on S -state quarkonia.

Our previous charmonium and bottomonium polarization calculations performed in the k_T -factorization approach [13, 14] describe both polarization and production at most p_T . However, the p_T dependence of the production calculation has a strong dependence on the factorization scale chosen. Also, the discrepancies between the ICEM polarization calculation and the measured data are not visualized in a frame-independent way. We address these issues in this paper by performing a polarized production calculation in the collinear factorization approach and also computing a frame-invariant polarization parameter to compare with the data. In this calculation, only the production and polarization of direct J/ψ is presented. We will address the effects of feed-down production on J/ψ in a later publication.

In this paper, we present both the yield and the polarization parameters of direct J/ψ production as a function

of p_T in the ICEM [12] using the collinear factorization approach. The polarized cross section calculation is presented in Sec. II. The results, along with comparison of unpolarized p_T distributions and polarization parameters to data, are shown in Sec. III. Our conclusions are presented in Sec. IV.

II. POLARIZED CROSS SECTION

The ICEM assumes the J/ψ production cross section takes a constant fraction of the open $c\bar{c}$ cross section with invariant mass above the mass of the J/ψ but below the hadron threshold, the $D\bar{D}$ pair mass. A distinction is also made between the $c\bar{c}$ momentum and the J/ψ momentum in the ICEM compared to the traditional CEM. The unpolarized direct J/ψ production cross section in $p + p$ collision in the ICEM is given by

$$\sigma = F_{J/\psi} \sum_{i,j} \int_{M_{J/\psi}}^{2m_D} dM dx_i dx_j f_i(x_i, \mu_F) f_j(x_j, \mu_F) \times \hat{\sigma}_{ij \rightarrow c\bar{c}+k}(p_{c\bar{c}}, \mu_R) \Big|_{p_{c\bar{c}} = \frac{M}{M_{J/\psi}} p_\psi}, \quad (1)$$

where i and j are q, \bar{q} and g such that $ij = q\bar{q}, qg, \bar{q}g$ or gg , $F_{J/\psi}$ is a universal factor at fixed order for direct J/ψ production in the ICEM independent of projectile and energy, x is the momentum fraction of the parton, and $f(x, \mu_F)$ is the parton distribution function (PDF) for a parton in the proton as a function of x and the factorization scale μ_F . Finally, $\hat{\sigma}_{ij \rightarrow c\bar{c}+k}$ are the parton-level cross sections for initial states ij to produce a $c\bar{c}$ pair with a light final-state parton k . The invariant mass of the $c\bar{c}$ pair, M , is integrated from the physical mass of J/ψ ($M_{J/\psi} = 3.10$ GeV) to two times the mass of the D^0 hadron ($2m_{D^0} = 3.72$ GeV). Because the $\mathcal{O}(\alpha_s^3)$ contribution diverges when the light parton is soft, in order to describe the p_T distribution at low J/ψ p_T , the initial-state partons are each given a small transverse momentum, k_T , kick of $\langle k_T^2 \rangle = 1 + (1/12) \ln(\sqrt{s}/20 \text{ GeV}) = 1.49 \text{ GeV}^2$ for $\sqrt{s} = 7 \text{ TeV}$. The collinear parton distribution functions

* Present address: Nuclear and Chemical Sciences Division, Lawrence Livermore National Laboratory, Livermore, California, 94551, USA.

are then multiplied by the Gaussian function $g(k_T)$,

$$g(k_T) = \frac{1}{\pi \langle k_T^2 \rangle} \exp(k_T^2 / \langle k_T^2 \rangle), \quad (2)$$

assuming the x and k_T dependences completely factorize. The same Gaussian smearing is applied in Refs. [12, 15, 16]. Note that in the traditional CEM, the lower invariant mass threshold for all charmonium states is set to the production threshold, which makes the kinematic distributions of the charmonium states identical except for the choice of F_Q . The distinction between the J/ψ and $c\bar{c}$ momenta also helps describe the p_T distributions at high p_T .

We consider diagrams with the projection operators, $\not{\epsilon}_\psi^*(J_z)(\not{p}_\psi + m_\psi)/(2m_\psi)$, applied to the $c\bar{c}$ [17, 18] to calculate the partonic cross sections. We denote the momenta of i , j , c , \bar{c} , and k in the partonic process $i + j \rightarrow c + \bar{c} + k$ are denoted as k_1 , k_2 , p_c , $p_{\bar{c}}$, and k_3 , respectively, where k is the emitted parton, with $\epsilon_1(S_{1z})$, $\epsilon_2(S_{2z})$, and $\epsilon_3(S_{3z})$ denoting the polarization of the light partons. When calculating the $2 \rightarrow 3$ cross section, we transformed the momenta of the charm quark

(p_c) and the anticharm quark ($p_{\bar{c}}$) into the momentum of the proto- J/ψ (p_ψ) and the relative momentum of the heavy quarks (k_r),

$$p_c = \frac{1}{2}p_\psi + k_r, \quad (3)$$

$$p_{\bar{c}} = \frac{1}{2}p_\psi - k_r, \quad (4)$$

and denote the polarization vector of the proto- J/ψ as $\epsilon_\psi(J_z)$, where J_z is the spin projection onto the polarization axis. Instead of taking the limit $k_r \rightarrow 0$, we note that, since the mass of the proto- J/ψ is integrated from the physical mass of J/ψ to the hadronic threshold, the relative momentum k_r depends on the mass of the proto- J/ψ .

We factorized the amplitudes into a product of the color factors, C , and the colorless amplitude \mathcal{A} , so that $\mathcal{M} = C\mathcal{A}$. The color factors, C , in the squared amplitudes are calculated separately by summing over all colors and averaging over the initial-state colors.

There are 16 diagrams for the $gg \rightarrow c\bar{c}g$ process. The factorized amplitudes, \mathcal{A} , arranged by the number of three-gluon vertices, are

$$\begin{aligned} \mathcal{A}_{gg0} &= ig_s^3 \text{tr} \left[\not{\epsilon}_2(\not{p}_c - \not{k}_2 + m_c) \not{\epsilon}_3^*(-\not{p}_{\bar{c}} + \not{k}_1 + m_{\bar{c}}) \not{\epsilon}_1 \not{\epsilon}_\psi^*(J_z) \frac{\not{p}_\psi + m_\psi}{2m_\psi} \right] \frac{1}{2p_c \cdot k_2} \frac{1}{2p_{\bar{c}} \cdot k_1} \\ &+ \text{five diagrams with no three - gluon vertices,} \end{aligned} \quad (5)$$

$$\begin{aligned} \mathcal{A}_{gg1} &= ig_s^3 \text{tr} \left[\not{\epsilon}_3^*(\not{p}_c + \not{k}_3 + m_c) \gamma^\mu \not{\epsilon}_\psi^*(J_z) \frac{\not{p}_\psi + m_\psi}{2m_\psi} \right] [(-k_1 - 2k_2) \cdot \epsilon_1 \epsilon_{2\mu} \\ &+ (\epsilon_1 \cdot \epsilon_2)(-k_1 + k_2)_\mu + (2k_1 + k_2) \cdot \epsilon_2 \epsilon_{1\mu}] \frac{1}{2p_c \cdot k_3} \frac{1}{(k_1 + k_2)^2} \\ &+ \text{five diagrams with one three - gluon vertex,} \end{aligned} \quad (6)$$

$$\begin{aligned} \mathcal{A}_{gg2} &= ig_s^3 \text{tr} \left[\gamma^\nu \not{\epsilon}_\psi^*(J_z) \frac{\not{p}_\psi + m_\psi}{2m_\psi} \right] [(-k_1 - 2k_2) \cdot \epsilon_1 \epsilon_2^\mu + (\epsilon_1 \cdot \epsilon_2)(-k_1 + k_2)^\mu \\ &+ (2k_1 + k_2) \cdot \epsilon_2 \epsilon_1^\mu] \\ &\times [(-k_1 - k_2 - p_\psi) \cdot \epsilon_3^* g_{\mu\nu} + \epsilon_3^*_\mu (k_3 + k_1 + k_2)_\nu + (p_\psi - k_3)_\mu \epsilon_3^*_{\nu}] \frac{1}{(k_1 + k_2)^2} \frac{1}{m_\psi^2} \\ &+ \text{two diagrams with two three - gluon vertices.} \end{aligned} \quad (7)$$

The diagram with a four-gluon vertex is factorized according to

$$\mathcal{M}_{gg4} = C_{gg4,1} \mathcal{A}_{gg4,1} + C_{gg4,2} \mathcal{A}_{gg4,2} + C_{gg4,3} \mathcal{A}_{gg4,3}, \quad (8)$$

with

$$\mathcal{A}_{gg4,1} = ig_s^3 \text{tr} \left[\gamma^\nu \not{\epsilon}_\psi^*(J_z) \frac{\not{p}_\psi + m_\psi}{2m_\psi} \right] (g_{\alpha\gamma} g_{\nu\beta} - g_{\alpha\beta} g_{\nu\gamma}) \frac{1}{m_\psi^2} \epsilon^\alpha \epsilon_2^\beta \epsilon_3^{*\gamma}, \quad (9)$$

$$\mathcal{A}_{gg4,2} = ig_s^3 \text{tr} \left[\gamma^\nu \not{\epsilon}_\psi^*(J_z) \frac{\not{p}_\psi + m_\psi}{2m_\psi} \right] (g_{\alpha\nu} g_{\gamma\beta} - g_{\alpha\beta} g_{\gamma\nu}) \frac{1}{m_\psi^2} \epsilon^\alpha \epsilon_2^\beta \epsilon_3^{*\gamma}, \quad (10)$$

$$\mathcal{A}_{gg4,3} = ig_s^3 \text{tr} \left[\gamma^\nu \not{\epsilon}_\psi^*(J_z) \frac{\not{p}_\psi + m_\psi}{2m_\psi} \right] (g_{\alpha\gamma} g_{\nu\beta} - g_{\alpha\nu} g_{\gamma\beta}) \frac{1}{m_\psi^2} \epsilon^\alpha \epsilon_2^\beta \epsilon_3^{*\gamma}. \quad (11)$$

There are five $gq \rightarrow c\bar{c}q$ diagrams, which, written in terms of Dirac spinors, are

$$\mathcal{A}_{gq,1} = -ig_s^3 \text{tr} \left[\gamma^\nu \not{\epsilon}_\psi^*(J_z) \frac{\not{p}_\psi + m_\psi}{2m_\psi} \right] [\bar{u}(k_3) \gamma_\nu (\not{k}_1 + \not{k}_2) \not{\epsilon}_1 u(k_2)] \frac{1}{m_\psi^2} \frac{1}{2k_1 \cdot k_2}, \quad (12)$$

$$\begin{aligned} \mathcal{A}_{gq,2} &= -ig_s^3 \text{tr} \left[\not{\epsilon}_1 (-\not{p}_c - \not{k}_1 + m_c) \gamma^\nu \not{\epsilon}_\psi^*(J_z) \frac{\not{p}_\psi + m_\psi}{2m_\psi} \right] [\bar{u}(k_3) \gamma_\nu u(k_2)] \\ &\times \frac{1}{-2p_c \cdot k_1} \frac{1}{(-k_3 + k_2)^2}, \end{aligned} \quad (13)$$

$$\begin{aligned} \mathcal{A}_{gq,3} &= -ig_s^3 \text{tr} \left[\gamma^\nu (\not{p}_{\bar{c}} + \not{k}_1 + m_c) \not{\epsilon}_1 \not{\epsilon}_\psi^*(J_z) \frac{\not{p}_\psi + m_\psi}{2m_\psi} \right] [\bar{u}(k_3) \gamma_\nu u(k_2)] \\ &\times \frac{1}{-2p_{\bar{c}} \cdot k_1} \frac{1}{(-k_3 + k_2)^2}, \end{aligned} \quad (14)$$

$$\begin{aligned} \mathcal{A}_{gq,4} &= -ig_s^3 \text{tr} \left[\gamma^\nu \not{\epsilon}_\psi^*(J_z) \frac{\not{p}_\psi + m_\psi}{2m_\psi} \right] [(k_3 - k_2 - p_\psi) \cdot \epsilon_{1g\mu\nu} + \epsilon_{1\mu}(-k_1 - k_3 + k_2)_\nu \\ &+ (p_\psi + k_1)_\mu \epsilon_{1\nu}] [\bar{u}(k_3) \gamma^\mu u(k_2)] \frac{1}{m_\psi^2} \frac{1}{(-k_3 + k_2)^2}, \end{aligned} \quad (15)$$

$$\mathcal{A}_{gq,5} = -ig_s^3 \text{tr} \left[\gamma^\nu \not{\epsilon}_\psi^*(J_z) \frac{\not{p}_\psi + m_\psi}{2m_\psi} \right] [\bar{u}(k_3) \not{\epsilon}_1 (\not{k}_3 - \not{k}_1) \gamma_\nu u(k_2)] \frac{1}{m_\psi^2} \frac{1}{-2k_1 \cdot k_2}. \quad (16)$$

There are five $g\bar{q} \rightarrow c\bar{c}\bar{q}$ diagrams, obtained by replacing the spinors in the above five $gq \rightarrow c\bar{c}q$ diagrams:

$$\mathcal{A}_{g\bar{q},1} = -ig_s^3 \text{tr} \left[\gamma^\nu \not{\epsilon}_\psi^*(J_z) \frac{\not{p}_\psi + m_\psi}{2m_\psi} \right] [\bar{v}(k_2) \not{\epsilon}_1 (-\not{k}_2 - \not{k}_1) \gamma_\nu v(k_3)] \frac{1}{m_\psi^2} \frac{1}{2k_1 \cdot k_2}, \quad (17)$$

$$\begin{aligned} \mathcal{A}_{g\bar{q},2} &= -ig_s^3 \text{tr} \left[\not{\epsilon}_1 (\not{p}_c - \not{k}_1 + m_c) \gamma^\nu \not{\epsilon}_\psi^*(J_z) \frac{\not{p}_\psi + m_\psi}{2m_\psi} \right] [\bar{v}(k_2) \gamma_\nu v(k_3)] \\ &\times \frac{1}{-2p_c \cdot k_1} \frac{1}{(-k_3 + k_2)^2}, \end{aligned} \quad (18)$$

$$\begin{aligned} \mathcal{A}_{g\bar{q},3} &= -ig_s^3 \text{tr} \left[\gamma^\nu (-\not{p}_{\bar{c}} + \not{k}_1 + m_c) \not{\epsilon}_1 \not{\epsilon}_\psi^*(J_z) \frac{\not{p}_\psi + m_\psi}{2m_\psi} \right] [\bar{v}(k_2) \gamma_\nu v(k_3)] \\ &\times \frac{1}{-2p_{\bar{c}} \cdot k_1} \frac{1}{(-k_3 + k_2)^2}, \end{aligned} \quad (19)$$

$$\begin{aligned} \mathcal{A}_{g\bar{q},4} &= -ig_s^3 \text{tr} \left[\gamma^\nu \not{\epsilon}_1 \not{\epsilon}_\psi^*(J_z) \frac{\not{p}_\psi + m_\psi}{2m_\psi} \right] [(k_3 - k_2 - p_\psi) \cdot \epsilon_{1g\mu\nu} \\ &+ \epsilon_{1\mu}(-k_1 - k_3 + k_2)_\nu + (p_\psi + k_1)_\mu \epsilon_{1\nu}] [\bar{v}(k_2) \gamma^\mu v(k_3)] \frac{1}{m_\psi^2} \frac{1}{(-k_3 + k_2)^2}, \end{aligned} \quad (20)$$

$$\begin{aligned} \mathcal{A}_{g\bar{q},5} &= -ig_s^3 \text{tr} \left[\gamma^\nu \not{\epsilon}_1 \not{\epsilon}_\psi^*(J_z) \frac{\not{p}_\psi + m_\psi}{2m_\psi} \right] [\bar{v}(k_2) \gamma_\nu (-\not{k}_3 + \not{k}_1) \not{\epsilon}_1 v(k_3)] \\ &\times \frac{1}{m_\psi^2} \frac{1}{-2k_3 \cdot k_1}. \end{aligned} \quad (21)$$

Finally, five diagrams contribute to $q\bar{q} \rightarrow c\bar{c}g$,

$$\begin{aligned} \mathcal{A}_{q\bar{q},1} = & -ig_s^3 \text{tr} \left[\gamma^\nu \not{\epsilon}_\psi^*(J_z) \frac{\not{p}_\psi + m_\psi}{2m_\psi} \right] [(-k_1 - k_2 - p_\psi) \cdot \epsilon_{3\mu}^* g_{\mu\nu} \\ & + \epsilon_{3\mu}^* (k_3 + k_1 + k_2)_\nu + (p_\psi - k_3)_\mu \epsilon_{3\nu}^*] [\bar{v}(k_2) \gamma^\mu u(k_1)] \frac{1}{m_\psi^2} \frac{1}{(k_1 + k_2)^2}, \end{aligned} \quad (22)$$

$$\begin{aligned} \mathcal{A}_{q\bar{q},2} = & -ig_s^3 \text{tr} \left[\not{\epsilon}_3^* (\not{p}_c + \not{k}_3 + m_c) \gamma^\nu \not{\epsilon}_\psi^*(J_z) \frac{\not{p}_\psi + m_\psi}{2m_\psi} \right] [\bar{v}(k_2) \gamma_\nu u(k_1)] \\ & \times \frac{1}{2p_c \cdot k_3} \frac{1}{(k_1 + k_2)^2}, \end{aligned} \quad (23)$$

$$\begin{aligned} \mathcal{A}_{q\bar{q},3} = & -ig_s^3 \text{tr} \left[\gamma^\nu (-\not{p}_{\bar{c}} - \not{k}_3 + m_c) \not{\epsilon}_3^* \not{\epsilon}_\psi^*(J_z) \frac{\not{p}_\psi + m_\psi}{2m_\psi} \right] [\bar{v}(k_2) \gamma_\nu u(k_1)] \\ & \times \frac{1}{2p_{\bar{c}} \cdot k_3} \frac{1}{(k_1 + k_2)^2}, \end{aligned} \quad (24)$$

$$\begin{aligned} \mathcal{A}_{q\bar{q},4} = & -ig_s^3 \text{tr} \left[\gamma^\nu \not{\epsilon}_\psi^*(J_z) \frac{\not{p}_\psi + m_\psi}{2m_\psi} \right] [\bar{v}(k_2) \gamma_\nu (-\not{k}_3 + \not{k}_1) \not{\epsilon}_3^* u(k_1)] \\ & \times \frac{1}{m_\psi^2} \frac{1}{-2k_1 \cdot k_3} \end{aligned}$$

$$\begin{aligned} \mathcal{A}_{q\bar{q},5} = & -ig_s^3 \text{tr} \left[\gamma^\nu \not{\epsilon}_\psi^*(J_z) \frac{\not{p}_\psi + m_\psi}{2m_\psi} \right] [\bar{v}(k_2) \not{\epsilon}_3^* (-\not{k}_2 + \not{k}_3) \gamma_\nu v(k_1)] \\ & \times \frac{1}{m_\psi^2} \frac{1}{-2k_2 \cdot k_3}. \end{aligned} \quad (25)$$

We assume that the angular momentum of the proto- J/ψ is unchanged by the transition from the parton level to the hadron level. We then convolute the partonic cross sections with the CT14 PDFs [19] in the domain where $p_\psi \cdot k = 0$. We restrict the partonic cross section calculations within the perturbative domain by introducing a regularization parameter such that all propagators are at a minimum distance of $Q_{\text{reg}}^2 = M^2$ from their poles, as employed in Ref. [17]. We take the factorization and renormalization scales to be $\mu_F/m_T = 2.1_{-0.85}^{+2.55}$ and $\mu_R/m_T = 1.6_{-0.12}^{+0.11}$ respectively, where m_T is the transverse mass of the charm quark produced ($m_T = \sqrt{m_c^2 + p_T^2}$, where $p_T^2 = 0.5\sqrt{p_{Tc}^2 + p_{T\bar{c}}^2}$). We also vary the charm quark mass around 1.27 ± 0.09 GeV. These variations were determined in Ref. [15], in which the uncertainties on the total charm cross section were considered.

III. POLARIZED PRODUCTION OF DIRECT J/ψ

We factor the polarization vector, $\epsilon_\psi(J_z)$, from the unsquared amplitudes for all sub processes, giving us the form

$$\mathcal{M}_n = \epsilon_\psi^\mu(J_z) \mathcal{M}_{n,\mu} \quad (26)$$

for each subprocess denoted by the initial states, $n = gg, gq, g\bar{q}, q\bar{q}$. The polarization vectors for $J_z = 0, \pm 1$ in the rest frame of the proto- J/ψ are

$$\epsilon_\psi(0)^\mu = (1, 0, 0, 0), \quad (27)$$

$$\epsilon_\psi(\pm 1)^\mu = \mp \frac{1}{\sqrt{2}} (0, 1, \pm i, 0), \quad (28)$$

using the convention that the fourth component is the z component. While the unpolarized cross section does not depend on the choice of z axis, the polarized cross sections does depend on the orientation of the z axis. In this calculation, the y axis is chosen to be the normal vector of the plane formed by the two beams with momenta \vec{P}_1 and \vec{P}_2 ,

$$\hat{y} = \frac{-\vec{P}_1 \times \vec{P}_2}{|\vec{P}_1 \times \vec{P}_2|}. \quad (29)$$

In the helicity frame, the z_{HX} axis is the flight direction of the $c\bar{c}$ pair in the center of mass of the colliding beams. In the Collins-Soper frame [20], the z_{CS} axis is the angle bisector between one beam and the opposite direction of the other beam. The x axis is then determined by the right-handed convention.

We compute the polarized cross section matrix element, \mathcal{M}_n , in the rest frame of the $c\bar{c}$ pair by first taking the product of the unsquared amplitude with polarization

vector of $J_z = i_z$ and the unsquared amplitude with polarization vector of $J_z = j_z$ in each subprocess (n), then adding them, and finally calculating the components of the polarized cross section matrix according to Eq. (1),

$$\sigma_{i_z, j_z} = \int \sum_n (\epsilon_{\psi}^{\mu}(i_z) \mathcal{M}_{n, \mu}) (\epsilon_{\psi}^{\nu}(j_z) \mathcal{M}_{n, \nu})^*, \quad (30)$$

where $i_z, j_z = \{-1, 0, +1\}$ and the integral is over all variables explicitly shown in Eq. (1) as well as the Lorentz-invariant phase space in $2 \rightarrow 3$ scatterings. The unpolarized cross section is the trace of the polarized cross section matrix

$$\sigma_{\text{unpol}} = \sum_{i_z} \sigma_{i_z, i_z} = \sigma_{-1, -1} + \sigma_{0, 0} + \sigma_{+1, +1}. \quad (31)$$

The polarization parameters are calculated using the matrix elements. The polar anisotropy (λ_{θ}), the azimuthal anisotropy (λ_{φ}), and polar-azimuthal correlation ($\lambda_{\theta\varphi}$) are given by [21]

$$\lambda_{\theta} = \frac{\sigma_{+1, +1} - \sigma_{0, 0}}{\sigma_{+1, +1} + \sigma_{0, 0}}, \quad (32)$$

$$\lambda_{\varphi} = \frac{\text{Re}[\sigma_{+1, -1}]}{\sigma_{+1, +1} + \sigma_{0, 0}}, \quad (33)$$

$$\lambda_{\theta\varphi} = \frac{\text{Re}[\sigma_{+1, 0} - \sigma_{-1, 0}]}{\sqrt{2}(\sigma_{+1, +1} + \sigma_{0, 0})}. \quad (34)$$

These parameters depend on the frame (helicity or Collins-Soper) in which they are calculated and measured. Since the angular distribution itself is rotationally invariant, there are ways to construct invariant polarization parameters from Eqs. (32)–(34). One of the combinations to form a frame-invariant polarization parameter ($\tilde{\lambda}$) is [21]

$$\tilde{\lambda} = \frac{\lambda_{\theta} + 3\lambda_{\varphi}}{1 - \lambda_{\varphi}}. \quad (35)$$

The choice of $\tilde{\lambda}$ is the same as the polar anisotropy parameter (λ_{θ}) in a frame where the distribution is azimuthally isotropic ($\lambda_{\varphi} = 0$). We can remove the frame-induced kinematic dependencies when comparing theoretical predictions to data by also considering the frame-invariant polarization parameter, $\tilde{\lambda}$.

IV. RESULTS

We first show how our approach describes the transverse-momentum-distributions of J/ψ compared to ALICE [22] and ATLAS [23] measurements at $\sqrt{s} = 7$ TeV and compare our results with previous calculations in the ICEM. We then discuss the transverse momentum and rapidity dependences of the frame-dependent polarization parameters λ_{θ} , λ_{φ} , and $\lambda_{\theta\varphi}$ as well as the frame-invariant polarization parameter $\tilde{\lambda}$ compared to the data measured by the LHCb Collaboration [24], the ALICE

Collaboration [25], and the CMS Collaboration [26]. In our calculations, we consider theoretical uncertainties by varying the charm quark mass, the renormalization scale, and the factorization scale as discussed in Sec. II. We also estimate the uncertainty on the fit parameter, $\delta F_{J/\psi}$. The total uncertainty band is then constructed by adding the mass and scale uncertainties in quadrature and varying $F_{J/\psi}$ from $F_{J/\psi} - \delta F_{J/\psi}$ to $F_{J/\psi} + \delta F_{J/\psi}$.

A. Unpolarized J/ψ p_T distribution

We calculate the p_T distribution of direct J/ψ production at $\sqrt{s} = 7$ TeV with $|y| < 0.9$. We assume direct production is a constant fraction, 0.62, of the inclusive production [27] to obtain the inclusive J/ψ p_T distribution. We compare our ICEM inclusive J/ψ p_T distribution with the data measured by the ALICE Collaboration [22]. The comparison is presented in Fig. 1. By comparing the total cross section for $p_T < 7$ GeV, we find $F_{J/\psi} = 0.0363$, consistent with previous CEM [15] and ICEM calculations [13]. We add the statistical and systematic uncertainties of the ALICE total cross section in quadrature. This results in a proportional uncertainty of 17% on the total cross section. Using the same proportional uncertainty, we estimate the uncertainty on $F_{J/\psi}$, $\delta F_{J/\psi}$ to be ± 0.0062 . We note that since this calculation is done using collinear factorization, the variation in the factorization scale does not result in a large uncertainty band as seen in our previous calculation using the k_T -factorization approach [13]. Overall, we have good agreement with the data over the p_T range measured.

We compare the ICEM inclusive J/ψ p_T distributions at $\sqrt{s} = 7$ TeV in the forward rapidity region covered by the ALICE detector, $2.5 < y < 4$ [22], and in the

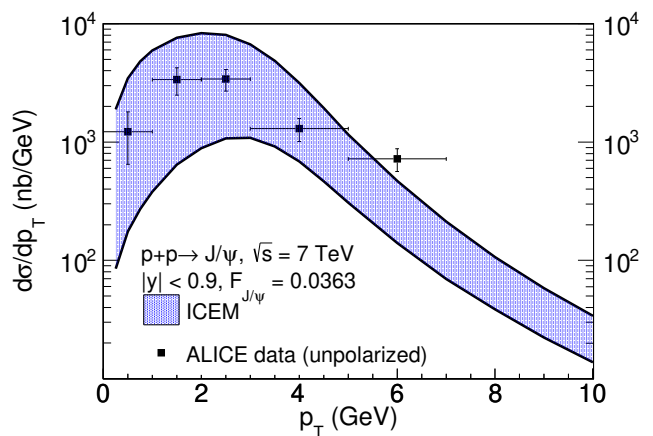


FIG. 1. The p_T dependence of inclusive J/ψ production at $\sqrt{s} = 7$ TeV with $|y| < 0.9$ in the ICEM. The combined mass, renormalization scale, factorization scale, and $F_{J/\psi}$ uncertainties are shown in the band and compared to the ALICE data [22]. The ALICE data are measured while assuming J/ψ production is unpolarized.

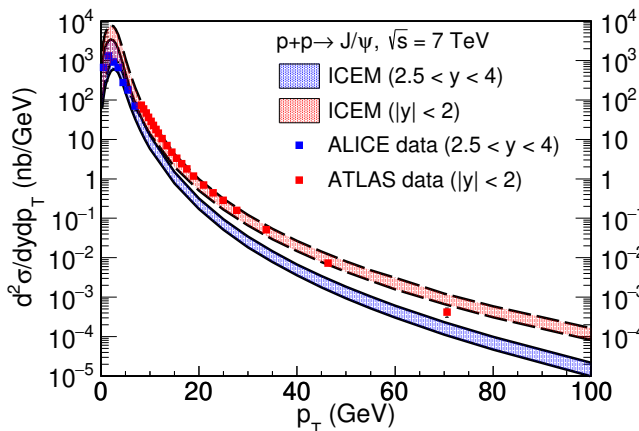


FIG. 2. The p_T dependence of inclusive J/ψ production at $\sqrt{s} = 7$ TeV with $2.5 < y < 4$ (blue region) and $|y| < 2$ in the ICEM (red region). The combined mass, renormalization scale, factorization scale, and $F_{J/\psi}$ uncertainties are shown in the band. They are compared to the ALICE data [22] (blue squares) and the ATLAS data [23] (red squares) respectively.

central rapidity region covered by the ATLAS detector, $|y| < 2$ [22]. These comparisons are presented in Fig. 2. Both ALICE and ATLAS data are shown assuming J/ψ production is unpolarized. Since the detector acceptance depends on the polarization assumption, the ATLAS Collaboration reports a set of correction factors for each polarization assumptions. These factors ranges from 0.7 to 1.7 for the lowest p_T bin, and from 0.90 to 1.06 for the highest p_T bin. Except for the highest p_T bin reported by the ATLAS Collaboration, we find our ICEM results in good agreement with the data over the p_T range measured in both kinematic regions using the same $F_{J/\psi}$ found by comparing to the ALICE central rapidity data.

We compare the p_T distribution of inclusive J/ψ production at $\sqrt{s} = 7$ TeV with $2 < y < 4.5$ in this calculation with that from previous calculations in the ICEM shown in Fig. 3. We compare these calculations with the data measured by the LHCb Collaboration [28]. Although this distribution is for unpolarized J/ψ , the calculation selects only $c\bar{c}$ with the same spin as the J/ψ . We thus refer to this calculation as polarized collinear ICEM. We compare this distribution with the polarized ICEM in the k_T -factorization approach [13] and the unpolarized ICEM in the collinear factorization approach [12]. The former also selects $c\bar{c}$ with the same spin as the J/ψ but the latter is a spin-averaged calculation. The uncertainty band of the unpolarized collinear ICEM is constructed in the same way as the polarized collinear ICEM. The uncertainty band of the k_T -factorized ICEM is constructed by varying the renormalization scale in the interval $0.5 < \mu_R/m_T < 2$ and varying the charm mass in the interval $1.2 < m_c < 1.5$. We find our polarized collinear ICEM p_T distribution behaves very similarly to the unpolarized collinear ICEM as p_T increases and agrees with the data and other calculations in the ICEM

in general.

B. p_T and y dependences of λ_ϑ , λ_φ , and $\lambda_{\vartheta\varphi}$

We calculate the p_T dependence of the frame-dependent polarization parameters λ_ϑ , λ_φ , and $\lambda_{\vartheta\varphi}$ at $\sqrt{s} = 7$ TeV in the helicity frame and in the Collins-Soper frame. We compare the polarization parameters at low and moderate p_T ($2 < p_T < 15$ GeV) with the data measured by the LHCb Collaboration [24] and the ALICE Collaboration [25], where the data are collected in rapidity ranges $2 < y < 4.5$ and $2.5 < y < 4$. The comparisons in the helicity frame and in the Collins-Soper frame are presented in Figs. 4 and 5, respectively. We then compare the polarization parameters at high p_T ($14 < p_T < 70$ GeV) with the data measured by the CMS Collaboration [25], where the data are collected in rapidity ranges $|y| < 0.6$ and $0.6 < |y| < 1.2$. These comparisons in the helicity frame and in the Collins-Soper frame are presented in Figs. 6 and 7, respectively.

The polar anisotropy parameter (λ_ϑ) reflects the proportion of the J/ψ in each spin projection state, with $\lambda_\vartheta = 1$ referring to completely transverse production of $J_z = \pm 1$ and $\lambda_\vartheta = -1$ referring to completely longitudinal production of $J_z = 0$. At low p_T , λ_ϑ is close to zero in both the helicity frame and the Collins-Soper frame, indicating equal J/ψ yields in each spin projection state ($J_z = 0, \pm 1$). However, as p_T grows larger, the difference between the λ_ϑ calculated in the two frames increases with p_T . In the helicity frame, the transverse component ($J_z = \pm 1$) falls off more slowly than the longitudinal

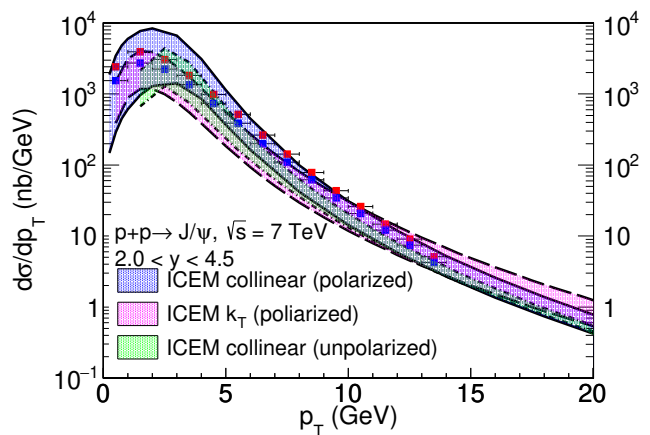


FIG. 3. The p_T dependence of inclusive J/ψ production at $\sqrt{s} = 7$ TeV in the polarized collinear ICEM (this calculation) (blue region), in the polarized ICEM using the k_T -factorization [13] (magenta region), in the unpolarized collinear ICEM [12] (green region). They are compared to the LHCb data [28] assuming that the J/ψ polarization is totally transverse, $\lambda_\vartheta = +1$ (red squares), and totally longitudinal, $\lambda_\vartheta = -1$ (blue squares). The LHCb data assuming $\lambda_\vartheta = 0$ lie between the red and blue points and are not shown.

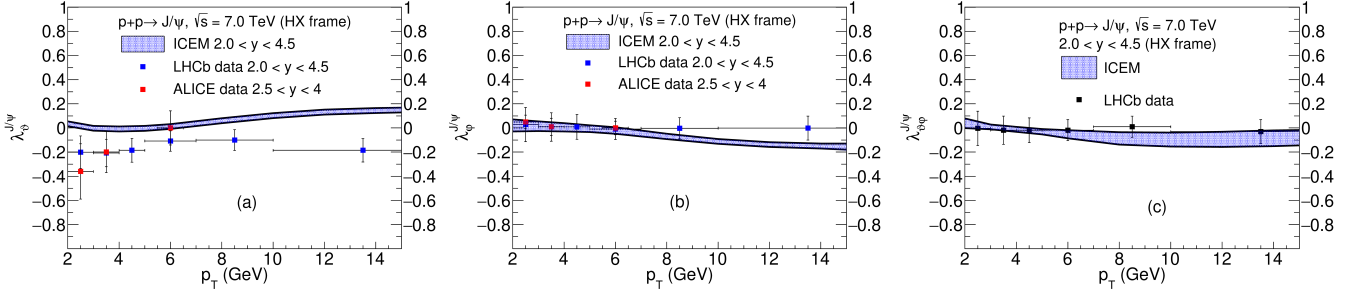


FIG. 4. (a) The polar anisotropy parameter (λ_θ), (b) the azimuthal anisotropy parameter (λ_φ), and (c) the polar-azimuthal correlation parameter ($\lambda_{\theta\varphi}$) (c) in the helicity frame at $\sqrt{s} = 7$ TeV in the ICEM. The combined mass, renormalization scale, and factorization scale uncertainties are shown in the band and compared to the LHCb data [24] (blue) and the ALICE data [25] (red).

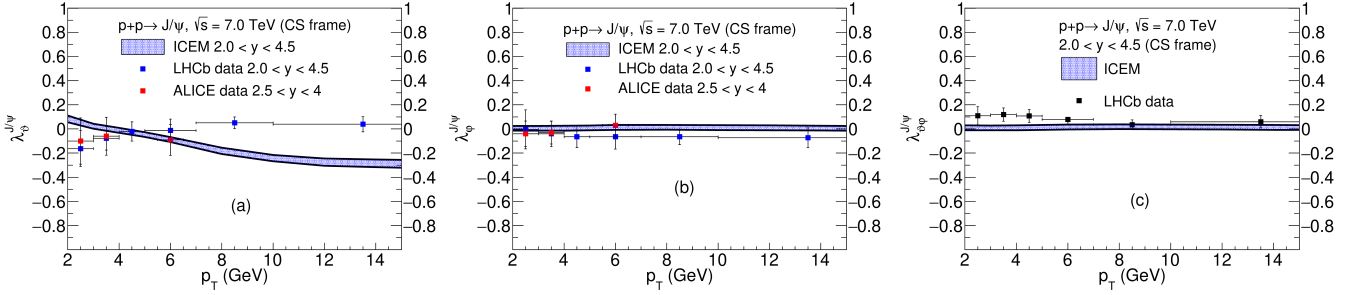


FIG. 5. (a) The polar anisotropy parameter (λ_θ), (b) the azimuthal anisotropy parameter (λ_φ), and (c) the polar-azimuthal correlation parameter ($\lambda_{\theta\varphi}$) (c) in the Collins-Soper frame at $\sqrt{s} = 7$ TeV in the ICEM. The combined mass, renormalization scale, and factorization scale uncertainties are shown in the band and compared to the LHCb data [24] (blue) and the ALICE data [25] (red).

component ($J_z = 0$). As a result, λ_θ becomes positive as p_T increases. This is consistent with the (color glass condensate) CGC+NRQCD approach at low and moderate p_T [29] and a NRQCD calculation at high p_T [30]. On the other hand, in the Collins-Soper frame, the longitudinal component dominates with increasing p_T . Thus, λ_θ becomes negative as p_T increases. This relative behavior of λ_θ in the two frames is expected because the polarization z axes are parallel at $p_T = 0$ and become orthogonal in the limit $p_T \rightarrow \infty$.

The azimuthal anisotropy parameter (λ_φ) reflects the azimuthal symmetry of J/ψ production. When $\lambda_\varphi = 0$, the production is azimuthally symmetric. When $\lambda_\varphi = \pm 1$, the azimuthal distribution is maximally asymmetric. We note that this parameter strongly depends on the production mechanism as well as the frame the distribution is measured in. In the Collins-Soper frame, this parameter is close to zero over all p_T as the matrix element $\sigma_{+1,-1}$ is small relative to $\sigma_{+1,+1}$ and $\sigma_{0,0}$. This means that the z_{CS} axis is approximately the azimuthal symmetry axis. In the helicity frame, the matrix element $\sigma_{+1,-1}$ is negative and become more negative. As a result, λ_φ becomes negative as p_T grows larger, showing that the z_{HX} axis is not the symmetry axis of the distribution. However, the distribution itself is rotationally invariant. The discrepancy between λ_φ in these two

frames is a combination of two factors: z_{CS} and z_{HX} becomes approximately orthogonal as p_T increases and production is not spherically symmetric.

The polar-azimuthal correlation parameter ($\lambda_{\theta\varphi}$) describes the angular correlation between 2θ and φ . When $\lambda_{\theta\varphi} = 0$, the two angles are uncorrelated and as $\lambda_{\theta\varphi}$ departs from 0, the behavior of the distribution becomes similar at locations where $2\theta = \varphi$. In both the helicity frame and the Collins-Soper frame, $\lambda_{\theta\varphi}$ is consistent with 0 at forward rapidity, which agrees with the data. At central rapidity, $\lambda_{\theta\varphi}$ pulls away from 0, but in general within the uncertainties of the data.

We observe a substantial rapidity dependence in the polarization parameters. To illustrate the rapidity dependence, we present the polarization parameters as a function of p_T in Fig. 8 in the most central rapidity and the forward rapidity regions covered by the CMS detector and the LHCb detector respectively. In both the Collins-Soper frame and in the helicity frame, the polar anisotropy parameter, λ_θ switches sign in the high p_T limit as rapidity increases. We observe a difference in the curvature of the polarized cross sections as a function of p_T in the forward rapidity region compared to the central rapidity region. At central rapidity, λ_θ becomes constant for $p_T \gtrsim 20$ GeV as the longitudinal and transverse cross sections fall off at similar rates while keeping

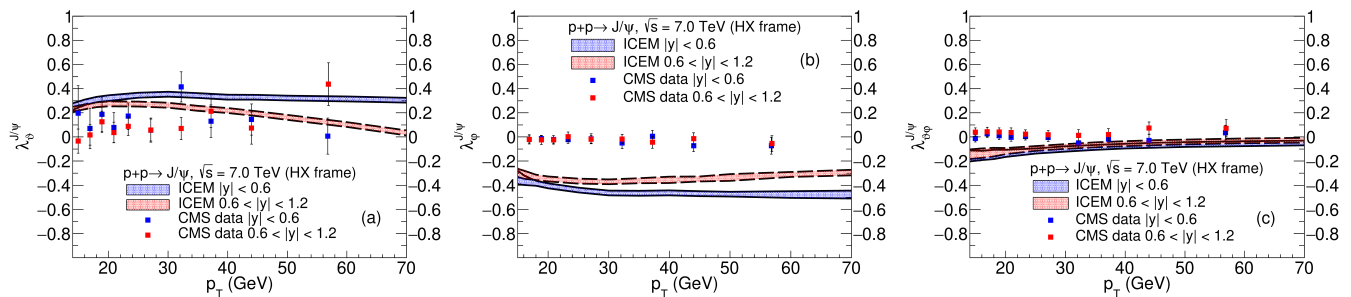


FIG. 6. (a) The polar anisotropy parameter (λ_θ), (b) the azimuthal anisotropy parameter (λ_φ), and (c) the polar-azimuthal correlation parameter ($\lambda_{\theta\varphi}$) in the helicity frame at $\sqrt{s} = 7$ TeV in the ICEM. The combined mass, renormalization scale, and factorization scale uncertainties are shown in the band and compared to the CMS data [26] in $|y| < 0.6$ (blue) and $0.6 < |y| < 1.2$ (red).

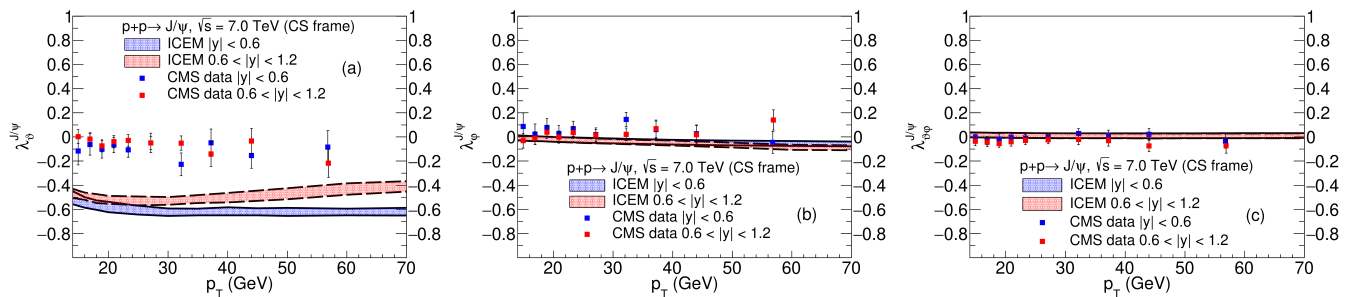


FIG. 7. (a) The polar anisotropy parameter (λ_θ), (b) the azimuthal anisotropy parameter (λ_φ), and (c) the polar-azimuthal correlation parameter ($\lambda_{\theta\varphi}$) in the Collins-Soper frame at $\sqrt{s} = 7$ TeV in the ICEM. The combined mass, renormalization scale, and factorization scale uncertainties are shown in the band and compared to the CMS data [26] in $|y| < 0.6$ (blue) and $0.6 < |y| < 1.2$ (red).

an approximately fixed ratio. At forward rapidity, in the Collins-Soper frame, the longitudinal cross section first falls off faster than the transverse cross section at moderate p_T , but at high p_T , the decrease of the longitudinal cross section slows down until it eventually dominates production. We observe the opposite behavior in the helicity frame, where the transverse cross section falls off more slowly than the longitudinal cross section and ultimately dominates production.

We also observe a rapidity dependence in λ_φ . At central rapidity, the polarized cross section matrix element, $\sigma_{+1,-1}$, from the gg contribution in the helicity frame is negative and relatively constant for $p_T \gtrsim 20$ GeV. As rapidity increases, the matrix element becomes smaller at moderate p_T and finally becomes small and positive at high p_T . Thus, λ_φ follows the gg contribution, and the production becomes more azimuthally symmetric with increasing rapidity. In the Collins-Soper frame, the azimuthal dependence of the distribution shows the opposite behavior as rapidity increases. Compared to at central rapidity, the magnitude of λ_φ at forward rapidity is larger at both moderate p_T and high p_T . As a result, the production becomes less azimuthally symmetric as rapidity increases. $\lambda_{\theta\varphi}$ is also rapidity dependent because the magnitude of the matrix element, $\sigma_{0,+1}$ in both frames is smaller at forward rapidity than at central rapidity. Note

that when the polarization parameters are close to zero, such as λ_φ and $\lambda_{\theta\varphi}$, the variation with rapidity is harder to visualize because a given fractional change in the size of a matrix element corresponds to a smaller change in the polarization parameter.

The resulting angular distributions in the helicity frame and in the Collins-Soper frame at $p_T = 12$ GeV are shown in Figs. 9(a) and 9(b), respectively. Note that two distributions are almost identical except that one appears to be rotated 90° with respect to the other. Thus, the two distributions can be interpreted as a top view and a side view of the production distributions. The angular distribution in the Collins-Soper frame, based on the data collected in the $10 < p_T < 15$ GeV bin by the LHCb Collaboration [24], is presented in Fig. 9(c).

We compare the polar anisotropy parameter, λ_θ , in this calculation with the one calculated in the polarized ICEM using the k_T -factorization approach [13] in Fig. 10. Since the k_T -factorized ICEM considers only the contribution from off-shell Reggeized gluons at $\mathcal{O}(\alpha_s^2)$, we compare the p_T dependence of λ_θ in the k_T -factorized ICEM with that in this calculation using the contribution from $gg \rightarrow c\bar{c}g$ at $\mathcal{O}(\alpha_s^3)$ only. The polarization calculated in the gg channel alone is approximately equivalent to that summed over all channels in the collinear factorization approach because the gg component dominates both

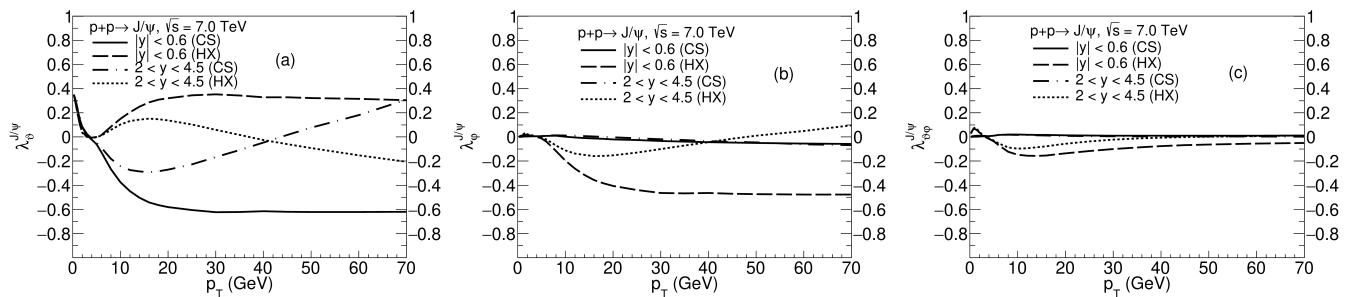


FIG. 8. (a) The polar anisotropy parameter (λ_θ), (b) the azimuthal anisotropy parameter (λ_φ), and (c) the polar-azimuthal correlation parameter ($\lambda_{\theta\varphi}$) at $\sqrt{s} = 7$ TeV in the ICEM. The ICEM results in the Collins-Soper frame in $|y| < 0.6$ (solid) and in $2 < y < 4.5$ (dot-dashed), and the results in the helicity frame in $|y| < 0.6$ (dashed) and in $2 < y < 4.5$ (dotted) are shown. Only the baseline results are shown here.

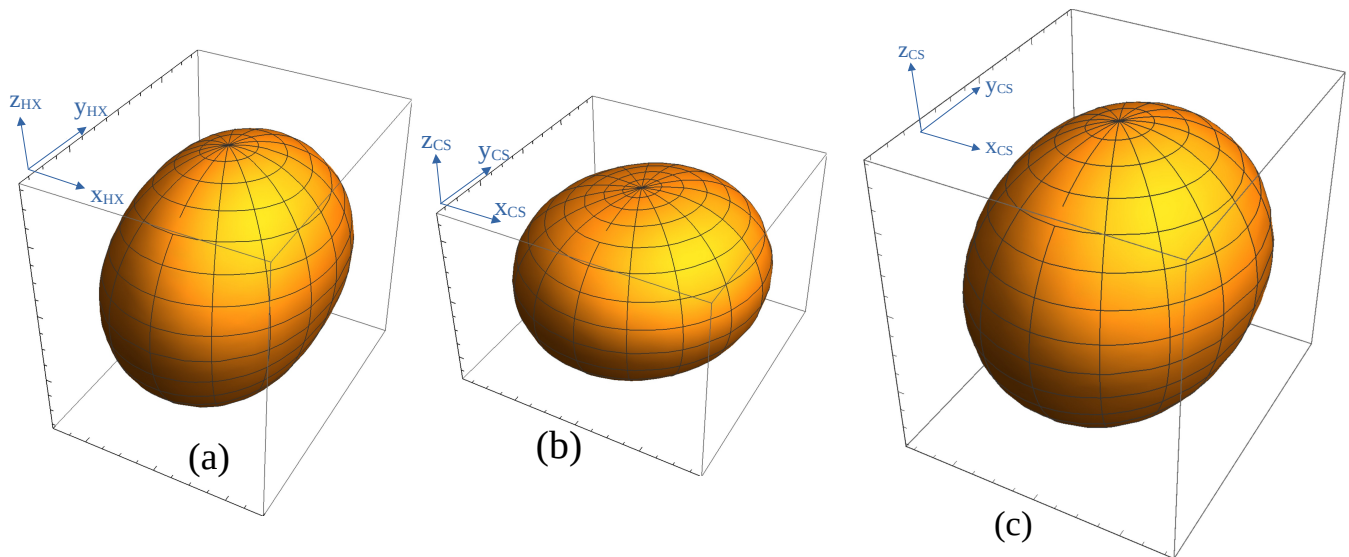


FIG. 9. (a) The angular distribution of the ICEM direct J/ψ production in the Collins-Soper frame and (b) in the helicity frame at $p_T = 12$ GeV. They represent the same angular distribution separated by one rotation. We constructed the angular distribution in the Collins-Soper frame based on the data collected in the $10 < p_T < 15$ GeV bin by the LHCb Collaboration [24], and it is shown in (c) for comparison.

the polarized and unpolarized cross sections. Although the kinematics in the two calculations are different, they both predict longitudinal polarization at high p_T , where the experimental results are nearly unpolarized. At small and moderate p_T , the difference in λ_θ is within the uncertainty of the data.

C. p_T and y dependence of $\tilde{\lambda}$

In Figs. 6 and 7, we observe that, at high p_T , the ICEM is in better agreement with the measured data in the helicity frame than in the Collins-Soper frame. However, even though we are switching from one frame to another, we are still comparing the same angular distributions. The difference between the ICEM polarization results and the data is then best quantified by a frame-independent polarization parameter. Thus, we compute

the frame-invariant polarization parameter $\tilde{\lambda}$ as a function of p_T using λ_θ and λ_φ . We compare $\tilde{\lambda}$ as a function of p_T with the data from LHCb and CMS in the helicity and the Collins-Soper frames in Fig. 11.

Since the azimuthal anisotropy parameter λ_φ in the Collins-Soper frame is close to zero in all p_T and y ranges considered, the p_T and y dependences of the invariant polarization parameter $\tilde{\lambda}$ are very similar to those in λ_θ of the Collins-Soper frame. We find the curves are generally within 1σ of the low and moderate p_T data, as shown in Fig. 11 (a). We also find the invariant polarization of direct J/ψ is relatively constant at high p_T . We observe a rapidity dependence similar to that of the λ_θ in the high p_T limit, where the invariant polarization is less longitudinal in the forward rapidity region than in the central rapidity region. We note that the invariant polarization parameter was devised as a way to treat each frame equally rather than to be the final arbiter between

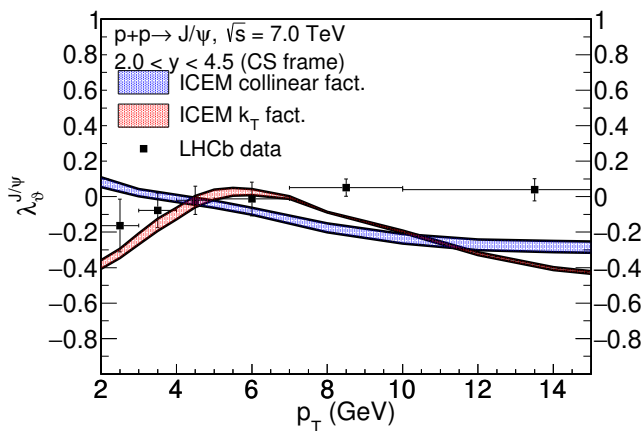


FIG. 10. The polar anisotropy parameter (λ_ψ) of direct J/ψ production at $\sqrt{s} = 7$ TeV with $2 < y < 4.5$ in the Collins-Soper frame calculated in the collinear ICEM in this work (blue) and in the k_T -factorized ICEM in Ref. [13]. Both calculations include only the gg contributions and are compared to the LHCb data [24].

theoretical model calculations. Our direct J/ψ -invariant polarization results are in reasonable agreement with the measured data over all p_T even though our calculations show a decrease in $\tilde{\lambda}$ with p_T . We note that including feed down from higher mass states could change the slope in this p_T range. Our results are in agreement with the J/ψ -invariant polarization found in the CGC+NRQCD approach at low and moderate p_T [29].

V. CONCLUSIONS

We have presented the transverse-momentum dependence of the direct J/ψ cross section as well as the polarization in $p + p$ collisions in the improved color evaporation model in the collinear factorization approach. We compare the p_T and y dependences to data for inclusive J/ψ production measured by the LHCb, ALICE, and CMS Collaboration. We also present the frame-invariant parameter, $\tilde{\lambda}$, as a function of p_T and compare our results with the data. We find direct J/ψ production is consistent with the unpolarized data at small and moderate p_T and becomes longitudinal in the high p_T limit. In the near future we will see if the feed-down contribution will have a positive influence on the parameter to match the data in that region. We will study the effects of feed-down production in this approach in a future publication.

VI. ACKNOWLEDGMENTS

This work was performed under the auspices of the U.S. Department of Energy by Lawrence Livermore National Laboratory under Contract No. DE-AC52-07NA27344 and supported by the U.S. Department of Energy, Office of Science, Office of Nuclear Physics (Nuclear Theory) under Contract No. DE-SC-0004014, and the LLNL-LDRD Program under Project No. 21-LW-034.

-
- [1] W. Caswell and G. P. Lepage, Phys. Lett. **167B**, 437 (1986).
[2] G. T. Bodwin, H. S. Chung, U. R. Kim, and J. Lee, Phys. Rev. Lett. **113**, 022001 (2014).
[3] P. Faccioli, V. Knünz, C. Lourenco, J. Seixas, and H. K. Wöhri, Phys. Lett. B **736**, 98 (2014).
[4] H. Han, Y. Q. Ma, C. Meng, H. S. Shao, and K. T. Chao, Phys. Rev. Lett. **114**, 092005 (2015).
[5] H. F. Zhang, Z. Sun, W. L. Sang, and R. Li, Phys. Rev. Lett. **114**, 092006 (2015).
[6] M. Neubert, Phys. Rep. **245**, 259 (1994).
[7] F. De Fazio, in *At the Frontier of Particle Physics/Handbook of QCD*, edited by M. A. Shifman (World Scientific, Singapore, 2000), p.1671.
[8] R. Casalbuoni, A. Deandrea, N. Di Bartolomeo, R. Gatto, F. Feruglio, and G. Nardulli, Phys. Rep. **281**, 145 (1997).
[9] V. D. Barger, W. Y. Keung, and R. J. N. Phillips, Phys. Lett. **91B**, 253 (1980).
[10] V. D. Barger, W. Y. Keung, and R. J. N. Phillips, Z. Phys. C **6**, 169 (1980).
[11] R. Gavai, D. Kharzeev, H. Satz, G. A. Schuler, K. Sridhar, and R. Vogt, Int. J. Mod. Phys. A **10**, 3043 (1995).
[12] Y. Q. Ma and R. Vogt, Phys. Rev. D **94**, 114029 (2016).
[13] V. Cheung and R. Vogt, Phys. Rev. D **98**, 114029 (2018).
[14] V. Cheung and R. Vogt, Phys. Rev. D **99**, 034007 (2019).
[15] R. E. Nelson, R. Vogt, and A. D. Frawley, Phys. Rev. C **87**, 014908 (2013).
[16] M. L. Mangano, P. Nason and G. Ridolfi, Nucl. Phys. **B373**, 295 (1992).
[17] S. P. Baranov, Phys. Rev. D **66**, 114003 (2002).
[18] E. L. Berger and D. L. Jones, Phys. Rev. D **23**, 1521 (1981).
[19] S. Dulat, T. J. Hou, J. Gao, M. Guzzi, J. Huston, P. Nadolsky, J. Pumplin, C. Schmidt, D. Stump and C. P. Yuan, Phys. Rev. D **93**, 033006 (2016).
[20] J. C. Collins and D. E. Soper, Phys. Rev. D **16**, 2219 (1977).
[21] P. Faccioli, C. Lourenco, J. Seixas, and H. K. Wöhri, Eur. Phys. J. C **69**, 657 (2010).
[22] K. Aamodt *et al.* (ALICE Collaboration), Phys. Lett. B **704**, 442 (2011); **718**, 692(E) (2012).
[23] G. Aad *et al.* (ATLAS Collaboration), Eur. Phys. J. C **76**, 283 (2016).
[24] R. Aaij *et al.* (LHCb Collaboration), Eur. Phys. J. C **73**, 2631 (2013).
[25] B. Abelev *et al.* (ALICE Collaboration), Phys. Rev. Lett. **108**, 082001 (2012).
[26] S. Chatrchyan *et al.* (CMS Collaboration), Phys. Lett. B **727**, 381 (2013).

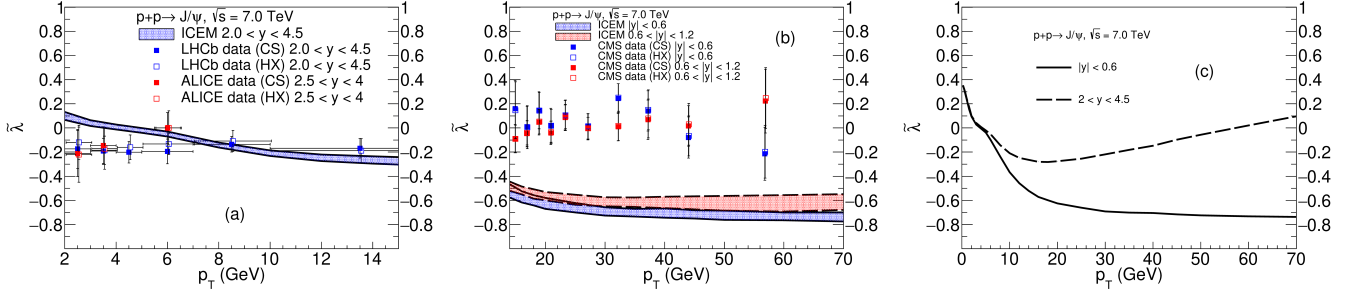


FIG. 11. The p_T dependence of the frame-invariant polarization parameter, $\tilde{\lambda}$, in the ICEM (a) compared to LHCb data [24] (blue) and the ALICE data [25] (red) at low p_T ; (b) compared to CMS data [26] in the most central rapidity bin (blue) and in the next rapidity bin (red) at high p_T ; and (c) the baseline ICEM results in $|y| < 0.6$ (solid) and $2 < y < 4.5$ (dashed). Data measured in the Collins-Soper frame are presented as solid points, and those in the helicity frame are presented as open points. The data in the helicity frame are displaced by 0.05 GeV for visualization purposes.

- [27] S. Digal, P. Petreczky, and H. Satz, *Phys. Rev. D* **64**, 094015 (2001).
 [28] R. Aaij *et al.* (LHCb Collaboration), *Eur. Phys. J. C* **71**, 1645 (2011).

- [29] Y. Q. Ma, T. Stebel, and R. Venugopalan, *J. High Energy Phys.* **12** (2018), 057.
 [30] K. T. Chao, Y. Q. Ma, H. S. Shao, K. Wang, and Y. J. Zhang, *Phys. Rev. Lett.* **108**, 242004 (2012).